Section 4

Parameterization of atmospheric and surface processes, effects of different physical parameterizations.

Improved SST–shortwave radiation feedback using an updated stratocumulus parameterization

CHIBA Jotaro[1] and KAWAI Hideaki[2]
[1]Numerical Prediction Division, Japan Meteorological Agency, Tsukuba, Japan
[2]Meteorological Research Institute, Japan Meteorological Agency, Tsukuba, Japan
(Email: jotaro-chiba@met.kishou.go.jp)

1 Introduction

The Japan Meteorological Agency (JMA) is developing the next-generation seasonal ensemble prediction system (JMA/MRI-CPS3; CPS3) to support three-month, warm-/cold-season and El Niño forecasts. The atmospheric physical processes of CPS3 are based on the operational JMA Global Spectral Model (GSM; JMA 2019) as of 2020, and an updated stratocumulus parameterization will be implemented to represent stratocumulus clouds in the atmospheric boundary layer. This report outlines the stratocumulus parameterization and presents the results of experiments focused on the feedback between sea surface temperature (SST) and shortwave radiation (SW) flux at the surface.

2 Stratocumulus parameterization

In a general circulation model it is difficult to represent explicitly the complex processes related to stratocumulus clouds, so our approach to tackling this issue involves diagnosing the inversion strength. Kawai and Inoue (2006) (K06) reported some simple conditions that are implemented in the current version of the GSM. A well-known index that corresponds reasonably well to low-level cloud amount is Estimated Inversion Strength (EIS; Wood and Bretherton, 2006). Kawai et al. (2017) proposed the Estimated Cloud Top Entrainment Index (ECTEI), which considers the water vapor profile in addition to EIS.

$$\mathrm{ECTEI} = \mathrm{EIS} - \beta L/C_\mathrm{p}\,(q_\mathrm{surf} - q_{700}) \qquad (1)$$

$$\beta = (1-k)C_\mathrm{qgap} \qquad (2)$$

where L is latent heat of evaporation; C_p is specific heat at constant pressure; q_surf and q_{700} are the specific humidity at the surface and 700 hPa, respectively; and k and C_qgap are constants.

In our new stratocumulus parameterization, when ECTEI is higher than a threshold, vertical diffusivity is weakened at the top of the boundary layer. As a result, the atmospheric boundary layer becomes wetter, and low clouds are then formed. The ECTEI corresponds more closely than EIS to the observed low-level cloud amount, and a reasonable cloud amount is represented, especially over the Southern Ocean, when the ECTEI is used in a parameterization (Kawai et al. 2019).

3 Experimental design

We conducted free-run experiments using an atmosphere–ocean coupled model. The resolution of the atmospheric model is TL319L100 (Δx ~ 55 km, top ~ 0.01 hPa); the resolution of the ocean model (MRI.COM ver4; Tsujino et al. 2017) is 0.25° × 0.25° with 60 vertical layers. We tested two stratocumulus schemes: one is similar to K06 (CNTL) and the other uses ECTEI (TEST). Calculation of the climatology and the correlation coefficient is based on the monthly mean value of a 30-year integration, excluding the first year as spin-up. Model output is evaluated against CERES-EBAF, COBE-SST and ISCCP data.

4 Results

Climatological low-level cloud amount during June–July–August (JJA) was higher in the TEST experiment than in CNTL, especially off the west coast of continents and over the Southern Ocean (Figure 1), which is consistent with Kawai et al. (2019).

Figure 2 shows the SST–SW feedback; shaded areas in warm (cold) colours indicate positive (negative) feedback. For example, in the positive-feedback region, when SST becomes higher the surface downward SW flux increases as a result of the decrease in cloud amount. CNTL failed to reproduce the widespread positive feedback over the subtropical ocean, whereas TEST represented it well. This is because for higher (lower) SST, q_surf in the second term on the right side of Equation (1) is generally larger (smaller); therefore,

ECTEI is smaller (larger) and as a result the parameterization gives less (more) low cloud. Kawai et al. (2017) proposed this mechanism to explain the spatial distribution of low cloud and the changes in different climates. This report confirms that the mechanism also works for the monthly variations in the present climate.

Negative feedback in the NINO.3 region seems to be better represented in TEST. It is, however, necessary to conduct much longer free-run experiments to evaluate phenomena related to El Niño–Southern Oscillation.

Acknowledgements

This work was supported in part by the Japan Society for the Promotion of Science (JSPS) KAKENHI (Grant Nos. JP18H03363, JP19K03977 and JP19H05699).

References

JMA, 2019: Outline of the operational numerical weather prediction at the Japan Meteorological Agency. Appendix to WMO technical progress report on the global data-processing and forecasting system and numerical weather prediction research. 188pp.

Kawai, H., and T. Inoue, 2006: A simple parameterization scheme for subtropical marine stratocumulus. *SOLA*, **2**, 17–20.

Kawai, H., T. Koshiro, and M. J. Webb, 2017: Interpretation of factors controlling low cloud cover and low cloud feedback using a unified predictive index. *J. Climate*, **30**, 9119–9131.

Kawai, H., et al., 2019: Significant improvement of cloud representation in the global climate model MRI-ESM2. *Geosci. Model Dev.*, **12**, 2875–2897.

Wood, R., and C. S. Bretherton, 2006: On the relationship between stratiform low cloud cover and lower-tropospheric stability. *J. Climate*, **19**, 6425–6432, doi:10.1175/JCLI3988.1.

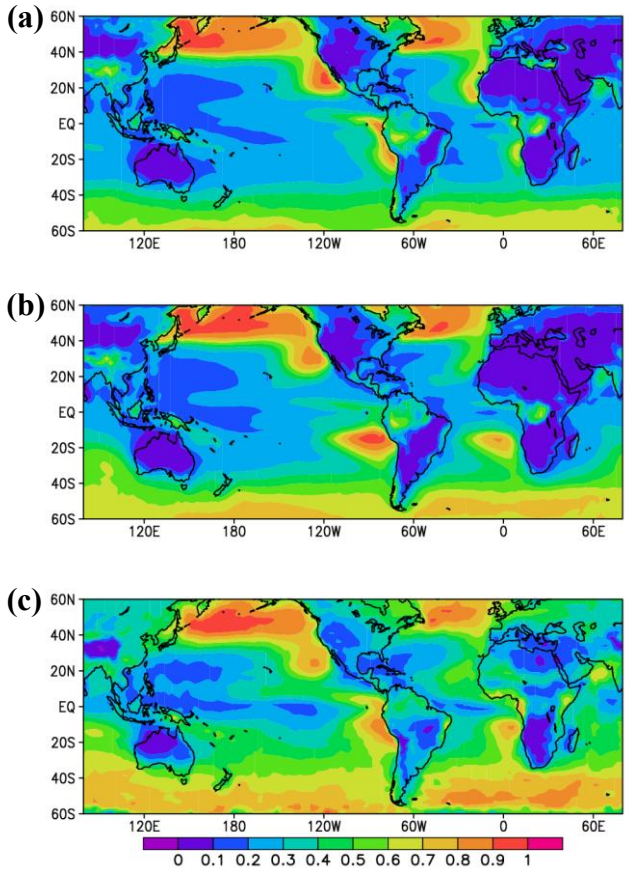

Figure 1 Climatology of low-level cloud amount during JJA for **(a)** CNTL **(b)** TEST and **(c)** ISCCP (1983–2008). ISCCP low-level cloud amount is calculated for areas free of middle- or upper-level clouds.

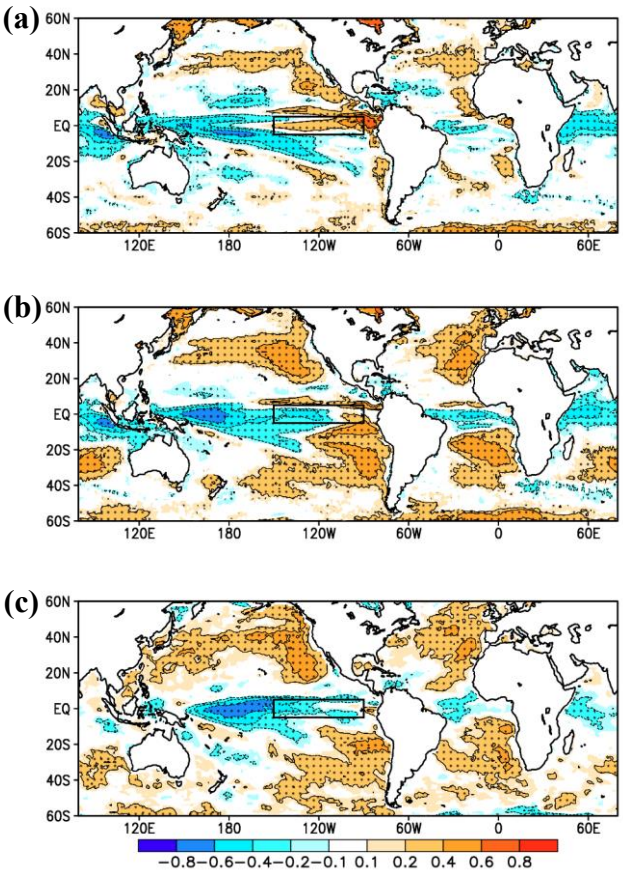

Figure 2 Correlation coefficient between SST and SW anomalies for all months. Anomalies are calculated with respect to the monthly climatology for **(a)** CNTL **(b)** TEST and **(c)** using COBE-SST and CERES-EBAF (2001–2015). Dotted areas are statistically significant at the 99% level. The black box is the NINO.3 region.

First and second derivatives for future use in AROME physics

by Rachel Honnert[1] *and Ryad El Khatib* [2]

[1]Météo-France. CNRM/GMAP. Toulouse. France.*E-mail: rachel.honnert@meteo.fr*
[2]Météo-France. CNRM/GMAP. Toulouse. France.*E-mail: ryad.elkhatib@meteo.fr*

1) Motivations - Introduction.

The AROME[7] numerical weather forecast model is a limited area model (LAM), whose code organization is based on the assumption that the best cost/benefit is gained from only treating the vertical sub-grid scale physical processes. Thus, the physical parameterizations do not have any information from neighboring columns. This organization allows a highly optimal distribution of the operations on the supercomputer. However, in recent years more and more parameterizations have appeared which require the use of horizontal gradients. They appear in particular with turbulence over complex terrain (cf. Goger et al.(2018)[3]), in deep convective clouds (cf. Verrelle et al.(2017)[8]) or at high resolution where the assumption of horizontal homogeneity may not be valid (cf. Honnert and Masson (2014)[4]). AROME would then lose the possible benefit of such parameterizations. The idea of this work is to recover the horizontal gradients calculated in the semi-Lagrangian dynamical scheme and to make them available for use in the physical parameterizations.

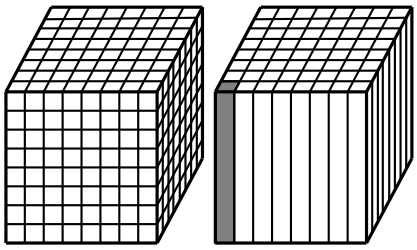

Figure 1: On the left, LAM 3D dynamical core. On the right, the purely vertical information transport in the model sub-grid parameterizations.

2) Computation

Geographic information does not exist in the physical part of the model. It does exist in the dynamic part, however, it is distributed on different processors according to Figure 2. The semi-Lagrangian advection scheme needs this information which circulates from one processor to another via a semi-Lagrangian halo (see Fig. 2 and IFS technical report[2] for more details). In the current work, the mechanism of the semi-Lagrangian halo has been used in order to compute horizontal gradients of all parameters (cf. Fig. 2). Only direct neighbors are need, thus the halo is one

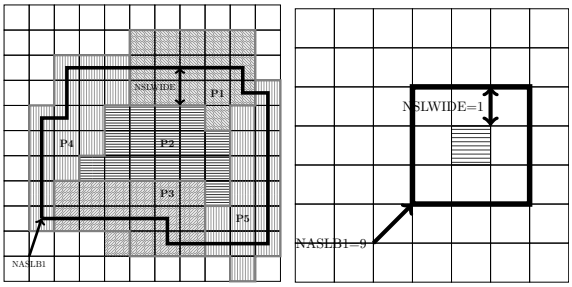

Figure 2: On the left, schematic representation of the semi-Lagrangian halo inspired from IFS technical report[2]. On the right, use of this semi-Lagrangian halo for computation of horizontal gradients. P1 to P5 represent groups of grid cells distributed on different processors. NSLWIDE is the width of the halo for P2 and NASLB1 is the total number of points.

grid space wide. The structure of the halo is defined as in the fullpos software[9]. However, the halo is used when the water mixing ratios (grid point parameters) are declared and computed, in order to be able to compute mixing ratio horizontal gradients as needed in Verrelle et al.(2017)[8]. Then, the horizontal gradients are transported from one routine to the next by the AROME physical interface.

3) First Results

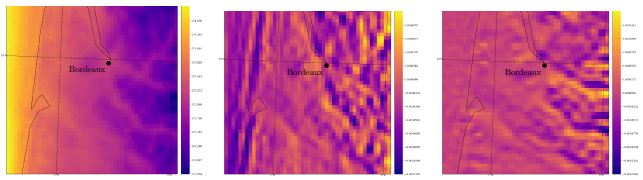

Figure 3: Temperature (T), $\frac{\partial T}{\partial x}$ and $\frac{\partial T}{\partial y}$ at the first level of the domain (April, 21st 2020)

The first tests have been made in a AROME toy model of 15 levels over the South-West of France, with 1, 2 and 4 processors. One can see the domain around the city of Bordeaux in Fig. 3, 4 and 5. All the parameters presented hereafter are computed in the dynamical core of the model and extracted in the AROME physical parameterization part. One can see that zonal and meridional horizontal gradients of potential temperature (Fig. 3) and water vapor mixing ratio (Fig. 5) are consistent, as well as the first and second order gradients of meridional wind (Fig. 4).

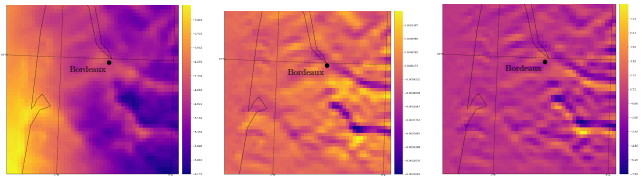

Figure 4: Idem Fig. 3 for the meridional wind (v), $\frac{\partial v}{\partial y}$ and $\frac{\partial^2 v}{\partial y^2}$

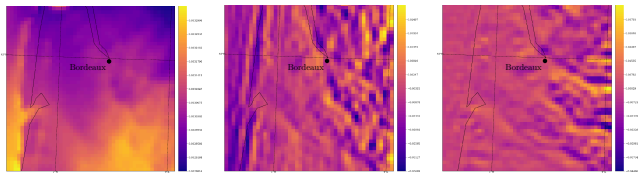

Figure 5: Idem Fig. 3 for water vapor mixing ratio (r_v), $\frac{\partial r_v}{\partial x}$ and $\frac{\partial r_v}{\partial y}$

Secondly, AROME cycle cy48 has been tested at 500 m and a time step of 15 s in a domain over the Alps (see Fig. 6) which is a difficult area of the France domain due to high mountains and steep slopes. It appears that the code modification is robust.

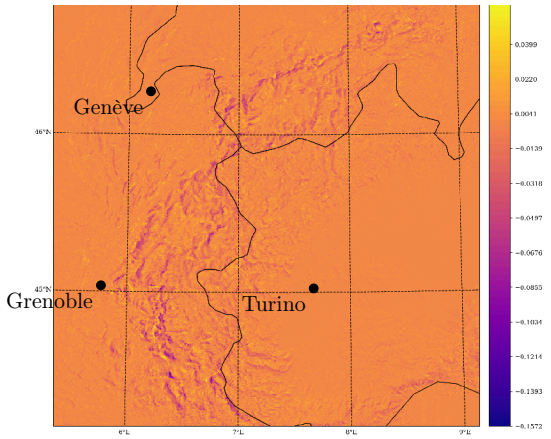

Figure 6: Wind divergence at around 40 m high (level 88).

4) Conclusions and Perspectives.

Over complex terrain at kilometre scales, the full three-dimensional effects have been found to be important in the shear production term for TKE (cf. Goger et al.(2018)[3]). Goger et al.(2018)[3] therefore proposes an extension of the 1D prognostic TKE equation used in the COSMO (COnsortium for Small-Scale Modeling) model turbulence scheme because that scheme otherwise underestimates the TKE. The 1D form considers only the contributions to shear production from vertical gradients of horizontal winds, but Goger et al.(2018)[3] supplement this with a further contribution of TKE containing horizontal gradients of the velocity. With the proposed changes, this is not very easily implementable. Otherwise, Verrelle et al.(2017)[8] propose to increase the mixing into the cumulus deep clouds by adding turbulence terms from Moeng et al.(2010)[6], which are horizontal gradients of the total mixing ratio and the potential temperature. Such gradients are not computed yet in the current version of the code. Finally, a complete transformation of the 1D turbulence scheme of AROME (cf. Cuxart et al.(2000)[1]) into a 3D scheme as in Meso-NH[5] would demand the computation of the horizontal divergence of the turbulence flux inside the physical parameterizations, which is not possible with this version of the code.

Acknowledgment I would like to acknowledge Fabrice Voitus for his precious advises in the computation of the parameters and Yann Seity for the creation of the "Alps" domain and "Sofog3D" domain used in the previous tests.

References

[1] Cuxart, C., P. Bougeault, and J.-L. Redelsperger, 2000: A turbulence scheme allowing for mesoscale and large-eddy simulations. *Quart. J. Roy. Meteor. Soc.*, **126**, 1–30.

[2] Cy45r1, 2019: Part vi: Technical and computational procedures. Tech. rep., IFS.

[3] Goger, B., M. W. Rotach, A. Gohm, O. Fuhrer, I. Stiperski, and A. A. M. Holtslag, 2018: The impact of three-dimensional effects on the simulation of turbulence kinetic energy in a major Alpine valley. *Boundary-Layer Meteorol.*, **168 (1)**, 1–27.

[4] Honnert, R., and V. Masson, 2014: What is the smallest physically acceptable scale for 1d turbulence schemes? *Front. Earth Sci.*, **2:27**, doi: 10.3389/feart.2014.00 027.

[5] Lac, C., and Coauthors, 2018: Overview of the Meso-NH model version 5.4 and its applications. *Geosci. Model Dev.*, **11**, 1929–1969.

[6] Moeng, C.-H., P. P. Sullivan, M. F. Khairoutdinov, and D. A. Randall, 2010: A mixed scheme for subgrid-scale fluxes in cloud-resolving models. *Journal of the Atmospheric Sciences*, **67 (11)**, 3692–3705, doi:10.1175/2010JAS3565.1.

[7] Seity, Y., P. Brousseau, S. Malardelle, G. Hello, F. Bouttier, C. Lac, and V. Masson, 2011: The AROME-France convective scale operational model. *Mon. Wea. Rev.*, **139**, 976–991.

[8] Verrelle, A., D. Ricard, and C. Lac, 2017: Evaluation and improvement of turbulence parameterization inside deep convective clouds at kilometer-scale resolution. *Mon. Wea. Rev.*, **145 (10)**, 3947–3967, doi:10.1175/MWR-D-16-0404.1.

[9] Yessad, K., 2011: Full-pos in the cycle 38 of arpege/ifs. Tech. rep., Meteo-France/CNRM/GMAP/ALGO.

Computation of moist-air surface entropy at Mauna Loa.

by Pascal Marquet.

CNRM, Université de Toulouse, Météo-France, CNRS, Toulouse. France. *E-mail: pascal.marquet@meteo.fr*

1) Motivations - Introduction.

Different assumptions exist for the calculation of the entropy of the atmosphere. A common practice in meteorology is to assume that the entropies of dry air and liquid water are zero at a pressure of $p_0 = 1000$ hPa and a temperature of $T_0 = 273.15$ K (0°C), leading to the "equivalent" version of the entropy defined with the reference values $s_{d0} = s_{l0} = 0$ (see for instance Pauluis *et al.*, 2010, Feistel. *et al.*, 2010).

In contrast, the usual practice in thermodynamics is to assume that "the entropies of all solids are zero for the most stable crystalline phase at 0 K" (the third law). Accordingly, the entropy for dry air at p_0 and T_0 is set to $s_{d0} \approx 6775$ J K^{-1} kg^{-1} in Hauf and Höller (1987) and Marquet (2011), $s_{d0} \approx 6776.1$ J K^{-1} kg^{-1} in Lemmon *et al.* (2000) and $s_{d0} \approx 6783$ J K^{-1} kg^{-1} in Stevens and Siebesma (2020). The more accurate value $s_{d0} \approx 6776.4$ J K^{-1} kg^{-1} is computed from the NIST-JANAF values at p_0 and T_0 (Chase, 1998).

The purpose of this note is to test some consequences of these hypotheses using CO_2 and surface atmospheric observations at the Mauna Loa observatory.

2) Dry-air values

Dry air is assumed to be composed of the four gases N_2, O_2, Ar and CO_2. The mole fractions (x) are taken from Table A2 in Feistel. *et al.* (2010) with 400 ppm (0.000400) for CO_2, 0.780848 for N_2, 0.209390 for O_2 and 0.009332 for Ar. The NIST-JANAF absolute (third-law) entropies at 1000 hPa and 273.15 K are (Chase, 1998): 6748.9 ± 0.7 J K^{-1} kg^{-1} for N_2, 6330.8 ± 1.1 J K^{-1} kg^{-1} for O_2, 3830.6 ± 0.1 J K^{-1} kg^{-1} for Ar and 4784.8 ± 2.7 J K^{-1} kg^{-1} for CO_2.

Fig. 1 (top) shows the change in CO_2 mole fraction at Mauna Loa over the period 1958 to 2020. The molar mass of dry air (M_d) increases over the period by 0.0015 g kg^{-1}, while the gas constant for dry air (R_d) decreases by 0.015 J K^{-1} kg^{-1}. These "constants" are thus variable, and one tenth of these changes may provide an idea of the accuracy of these M_d and R_d values for a given decade. The blue dashed lines represent the values for 400 ppm retained in Feistel. *et al.* (2010).

The bottom panel in Fig. 1 shows the changes in absolute (red+black) and "equivalent" (blue+violet) dry-air entropies computed according to the formula:

$$s_{d0} = \sum_k x_k \, s_{k0} \; - \; \sum_k x_k \, \ln(x_k) \, R_k \, , \qquad (1)$$

where x_k are the molar concentrations, s_{k0} the reference entropies, and $R_k = R/M_k$ the gas constants for each gases k, with $R \approx 8.314472$ J K^{-1} kg^{-1}. The "equivalent" value is computed here with zero reference entropies $s_{k0} = 0$ but with a non-zero contribution from the second sum in (1), which depends on the partial pressures $x_k \, p_0$. A stricter definition that imposes a zero value of s_{d0} (Pauluis *et al.*, 2010, Feistel. *et al.*, 2010) corresponds to the constant green line. The absolute value is computed with the third-law reference values indicated above. The 2015 value ≈ 6776.38 J K^{-1} kg^{-1} for 400 ppm is close to the one computed with the standard NIST-JANAF values.

The absolute and equivalent formulations evolve differently over the period, one increasing while the other decreases, with a difference reaching +0.3 J K^{-1} kg^{-1} in 2020 (+0.08 J K^{-1} kg^{-1} for the stricter definition). Since time variations of opposite sign have no physical meaning, only the absolute value of the entropies should be considered, as this alone corresponds to the definition given in thermodynamics.

3) Moist-air values

The entropy of moist air was calculated from hourly averages of temperature, pressure and humidity at 2m at Mauna Loa. The absolute water-vapour entropy at p_0 and T_0 if the NIST-JANAF third-law value $s_{d0} \approx 10318 \pm 2$ J K^{-1} kg^{-1}. Figure 2 shows that if the temperature increases by more than 1 K on average over this period between 1977 and 2019, the pressure decreases by about 1 hPa and the water vapour content increases by about 0.4 g kg^{-1}. The larger monthly and annual variations can reach 2 K, 2 hPa and 2 g kg^{-1}.

The impact on the moist-air entropy (for the average trend over the period as well as for the monthly variations) is, again, of a different nature if one considers the absolute (red) or "equivalent" (blue) definitions of the moist-air entropy. The impact of water-vapour variations is clearly overestimated with the "equivalent" version, which is therefore not *equivalent* to the thermodynamic absolute definition of entropy.

4) Conclusions.

The data observed at Mauna Loa show: 1) that the quantities M_d and R_d should not be constants in weather forecasting and climate models; 2) that the entropy of both dry and moist air varies differently from what thermodynamics predicts if the "equiva-

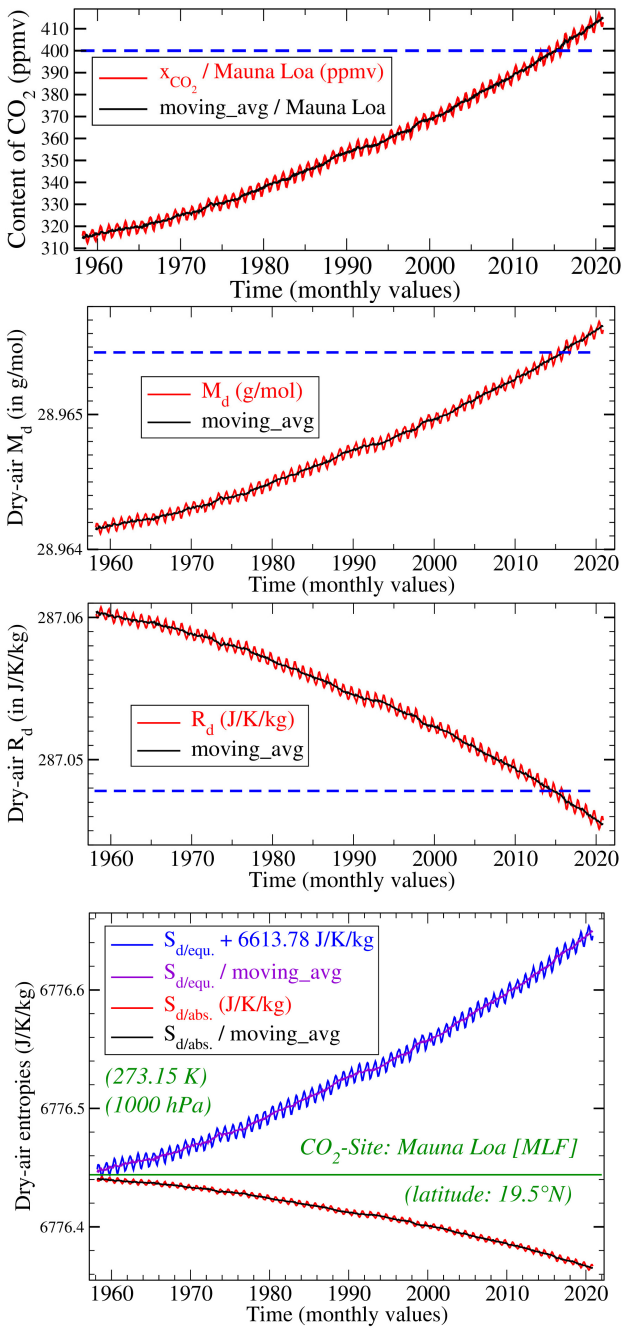

Figure 1: *Change in several dry-air physical properties at Mauna Loa between 1958 and 2020 (monthly means).*

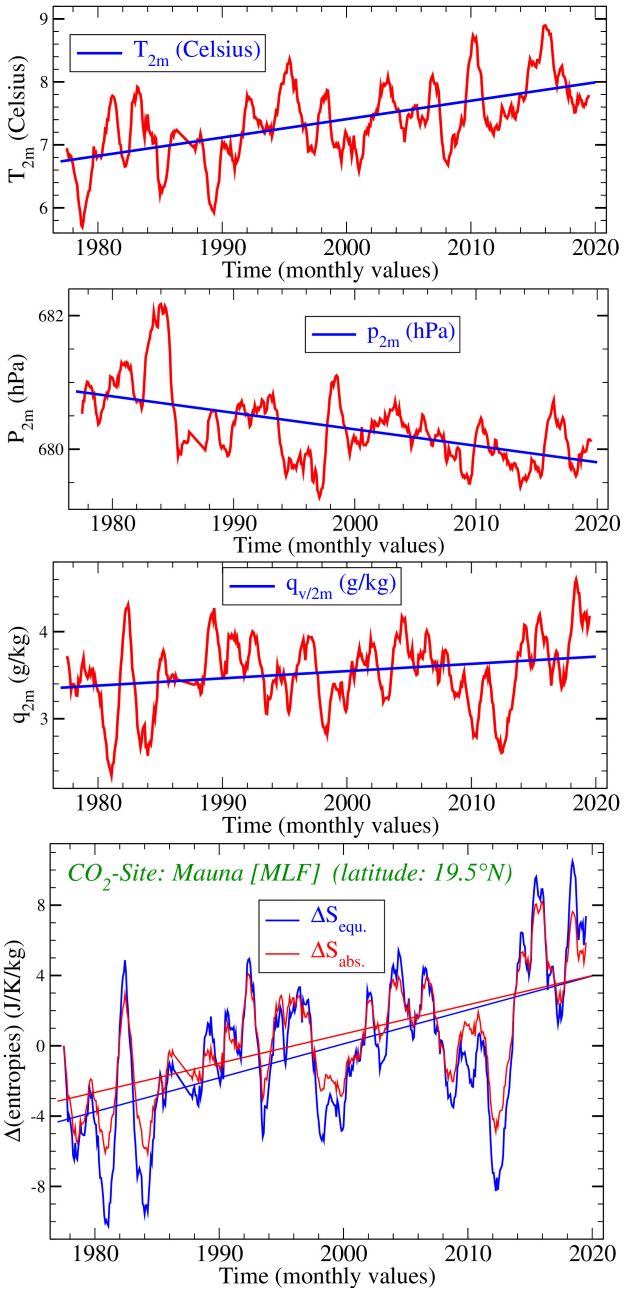

Figure 2: *Change in several moist-air physical properties at Mauna Loa between 1977 and 2019 (hourly means).*

lent" value is considered; 3) and therefore with the need to take into account the absolute definition of the moist-air entropy, which can be easily calculated from the third law and the NIST-JANAF dataset.

Acknowledgements

Monthly means and de-seasonalized CO2 concentration at Mauna Loa are from Pieter Tans, NOAA/GML (`www.esrl.noaa.gov/gmd/ccgg/trends/`) and Dr. Ralph Keeling, Scripps Institution of Oceanography (`scrippsco2.ucsd.edu/`). Meteorology Measurements are from the NOAA/ESRL/GMD Baseline Observatories (Brian Vasel, Boulder, Colorado, brian.vasel@noaa.gov).

References

• Chase, M. W., (1998). *Journal of physical and chemical reference data. Monograph No9.*, NIST-JANAF thermochemical tables. Fourth Edition. American Chemical Society and American Institute of Physics.

• Feistel R., Wright D.G., Kretzschmar H.-J., Hagen E., Herrmann S., Span R. (2010). Thermodynamic properties of sea air. *Ocean Sci.*., **6**: 91-141.

• Hauf T. and Höller H. (1987). Entropy and potential temperature. *J. Atmos. Sci.*, **44**: 2887–2901.

• Lemmon W.E., Jacobsen R.T., Penoncello S.G., Friend D.G. (2000). Thermodynamic Properties of Air and Mixtures of Nitrogen, Argon, and Oxygen From 60 to 2000 K at Pressures to 2000 MPa. *J. Phys. Chem. Ref. Data*, **29**: 331-385.

• Marquet P. (2011). Definition of a moist entropic potential temperature. Application to FIRE-I data flights. *Q. J. R. Meteorol. Soc.*, **137**: 768-791. `https://arxiv.org/abs/1401.1097`

• Pauluis O., Czaja A., Korty, R. (2010). The Global Atmospheric Circulation in Moist Isentropic Coordinates. *J. Clim.*, **23**: 3077–3093.

• Stevens B. and Siebesma A.P. (2020). *Clouds as Fluids*. In A. Siebesma, S. Bony, C. Jakob, & B. Stevens (Eds.), Clouds and Climate: Climate Science's Greatest Challenge (pp. 35-73). Cambridge: Cambridge University Press.

Comparisons of H_2O pathways with moist isentropes.

by Pascal Marquet[1] *and Adriana Bailey*[2]

[1]CNRM, Université de Toulouse, Météo-France, CNRS, Toulouse. France. *E-mail: pascal.marquet@meteo.fr*
[2]Earth Observing Laboratory. National Center for Atmospheric Research. USA. *E-mail: abailey@ucar.edu*

1) Motivations - Introduction.

A moist isentropic framework is used in Bailey *et al.* (2019, hereafter B19) to study poleward moisture transport in the atmosphere. In this work, it was demonstrated that the moisture plumes evaporated from 10° bands of latitude from the subtropics poleward approximately align with the "moist-air isentropic surfaces," as measured by the first-order approximation of the equivalent potential temperature:

$$\theta_e \approx \theta \, \exp\left(\frac{L_v \, r_v}{c_{pd} \, T}\right) \approx \theta \left(1 + \frac{L_v \, r_v}{c_{pd} \, T}\right) \approx \theta + \frac{L_v \, r_v}{c_{pd}} \, ,$$

where T is the absolute temperature, p is the pressure, $p_0 = 1000$ hPa, $\theta = T \, (p_0/p)^\kappa$ is the dry-air potential temperature with $\kappa \approx 0.285$, $c_{pd} \approx 1006$ J K^{-1} kg^{-1} is the dry-air specific heat at constant pressure, $L_v \approx 2500$ kJ kg^{-1} is the latent heat of vaporization and r_v is the water-vapour mixing ratio.

However, as demonstrated for the 30°S to 40°S latitude band in Fig. 1 (Fig.1e of B19), the colored moisture plume exhibits a southward shift from $\theta_e \approx 310$ K below 850 hPa to $\theta_e \approx 300$ K above 500 hPa, indicating some degree of "cross-isentropic" transport which may be interpreted as a "diabatic" decrease of θ_e through water loss through precipitation or radiative cooling (OLR).

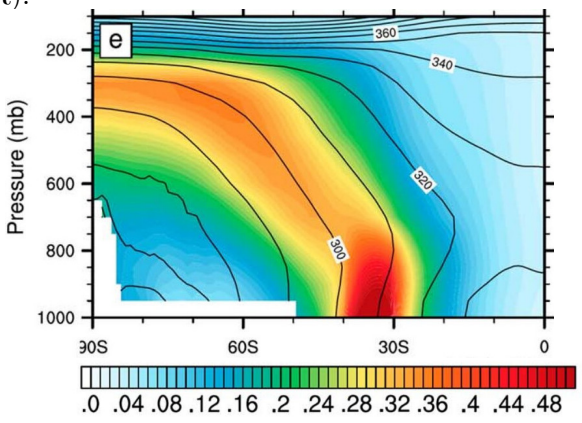

Figure 1: *The Fig.1e of B19. Normalized, annual and zonal mean distributions of water vapor in the Southern Hemisphere sourced from 30°S to 40°S, overlain with equivalent potential temperature θ_e contours (K). All variables come from a fully coupled Community Earth System Model.*

It is shown in this note that the way the isentropes are measured matters in the interpretation of "cross-isentropic" transport and that, in fact, this "cross-isentropic" transport almost vanishes if the absolute definition of moist-air entropy is used instead of equivalent potential temperature.

2) The absolute moist-air entropy.

Absolute definitions of reference entropies of dry air and water vapour have been considered in atmospheric science by Hauf and Höller (1987), Marquet (2011) and Stevens and Siebesma (2020), with a recent application in the IFS model described in Marquet and Bechtold (2020). The first-order approximation of the corresponding potential temperature θ_s is computed in Marquet (2011):

$$\theta_s \;\approx\; \theta \, \exp\left(-\frac{L_v \, q_l}{c_{pd} \, T} \;-\; \frac{L_s \, q_i}{c_{pd} \, T} \;+\; \Lambda \, q_t\right) \, , \qquad (1)$$

where $\kappa \approx 0.2857$, $c_{pd} \approx 1004.7$ J K^{-1} kg^{-1}, q_l, q_i and $q_t = q_v + q_l + q_i$ are the liquid-water, ice and total water specific contents, respectively, $L_s \approx 2835$ kJ kg^{-1} is the latent heat of sublimation and $\Lambda = (s_{vr} - s_{dr})/c_{pd} \approx 5.87$ is the key value depending on the absolute definitions of the reference entropies $s_{vr} \approx 12673$ J K^{-1} kg^{-1} and $s_{dr} \approx 6777$ J K^{-1} kg^{-1} .

3) Comparison of moist-air isentropes

Fig. 2 shows the same moisture plume and contours of θ_e (solid lines) as in Fig. 1, but with the new contours of θ_s added (dashed lines). Since the moisture plume almost follows the $\theta_s = 300$ K contour, the "cross-isentropic" transport almost vanishes with the absolute-entropy potential temperature θ_s.

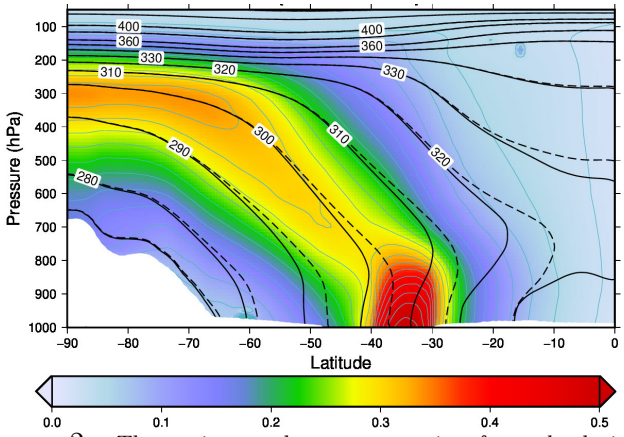

Figure 2: *The moisture plume evaporating from the latitude band 30°S to 40°S with the isentropes computed using either θ_e (solid lines) or with the new absolute moist-air entropy potential temperature θ_s (dashed lines).*

The isentropic means of the moisture plume of Fig. 2 are depicted in Figs. 3 as a function of height. They are computed according to Eq.(1) of Pauluis and Mrowiec (2013) for each bin of 1 K for both θ_e (top) and θ_s (bottom), with computations adapted here to the latitude and pressure coordinates.

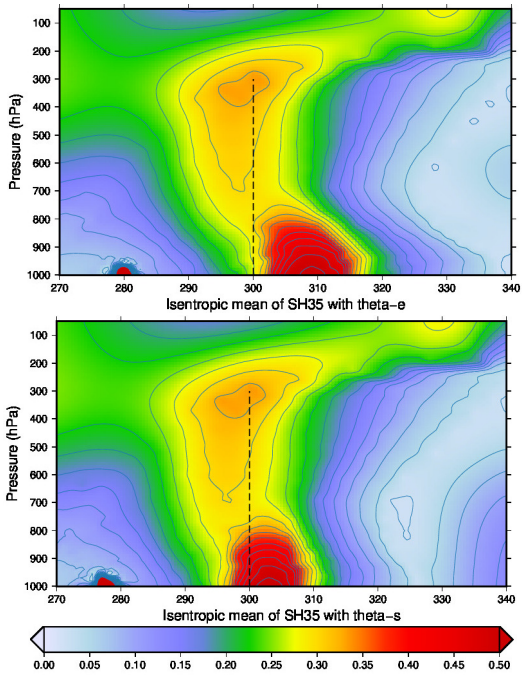

Figure 3: *"Isentropic means" of the moisture plume of Fig. 2 averaged over "isentropic surfaces" for θ_e (top) and θ_s (bottom).*

Clearly, the impact of the diabatic heating rate $\dot{Q}$ defined from the absolute entropy equation $d\theta_s/dt = \dot{Q}/T$ and due to radiation, evaporation, precipitations and irreversible changes of phases, is smaller for θ_s than for the alternative definitions based on the "equivalent" values $d\theta_e/dt$ and θ_e

This feature can be better understood with the definition $s(\theta_s) = c_{pd} \ln(\theta_s) + s_{ref}$ of Marquet (2011, Eq. 59), where θ_s is directly linked to the absolute moist-air entropy $s(\theta_s)$ by a simple relation where $s_{ref} \approx 1139$ J K^{-1} kg^{-1} is a constant and c_{pd} is the same constant as in Eq. (1). The link $s(\theta_e) \approx c_{pm}(q_t) \ln(\theta_e/T_0)$ between θ_e and $s(\theta_e)$ is more complicated (Eq. 13 of Marquet, 2017, with $T_0 = 273.15$ K), because it involves additional term depending on changes on q_t in the moist-air value $c_{pm} = c_{pd} + (c_l - c_{pd})\, q_t$, where $c_l \approx 4218$ J K^{-1} kg^{-1} is the liquid-water value. According to Eq. 48 of Marquet and Geleyn (2015) and Eq. 6 of Marquet and Dauhut (2018), changes in θ_s and θ_e are given by

$$\frac{c_{pd}}{\theta_s}\,\frac{d\theta_s}{dt} = \frac{ds}{dt} = \frac{\dot{Q}}{T}\,, \tag{2}$$

$$s(\theta_e) = s(\theta_s) + (s_{dr} - s_{lr})\; q_t \;-\; s_{dr}\,, \tag{3}$$

$$\frac{c_{pm}}{\theta_e}\,\frac{d\theta_e}{dt} = \frac{\dot{Q}}{T} + \left[\, s_{dr} - s_{lr} - (c_l - c_{pd})\,\frac{s(\theta_e)}{c_{pm}}\right]\frac{dq_t}{dt}\,, \tag{4}$$

where $s_{lr} \approx 3517$ J K^{-1} kg^{-1} is the reference absolute entropy of liquid water.

For varying total water content and $dq_t/dt \neq 0$ like in the moisture plumes in Figs. 2 and 3, the additional bracketed terms in Eq. (4) prevent a clear interpretation of $d\theta_e/dt$, as compared to the sole diabatic term $\dot{Q}/T$ in Eq. (2). The impact of the positive bracketed term should explain why the moisture plume does not follow contours of θ_e, if the physical processes almost lead to a conservation of θ_s. More precisely, for $d\theta_s/dt \approx 0$ and thus $\dot{Q} \approx 0$, if q_t decreases with height then $dq_t/dt < 0$ and $d\theta_e/dt < 0$, with indeed a decrease in θ_e by about 10 K from the surface to 400 hPa in the figures.

4) Conclusions.

The results of this note show that the way in which the moist-air isentropes are defined and calculated has a strong influence on the interpretation of cross-isentropic and diabatic processes in the study of poleward atmospheric moisture transport.

The absolute definition of entropy and the use of the associated variable θ_s, instead θ_e, leads to original, simpler and more accurate physical interpretations.

Acknowledgements

This material is based upon work supported by the National Center for Atmospheric Research, which is a major facility sponsored by the National Science Foundation under Cooperative Agreement No. 1852977.

References

• Bailey A., Singh H. K. A. and Nusbaumer J. (2019). Evaluating a moist isentropic framework for poleward moisture transport: Implications for water isotopes over Antarctica. *Geophysical Research Letters*, **46**: 7819–7827.

• Hauf T. and Höller H. (1987). Entropy and potential temperature. *J. Atmos. Sci.*, **44**: 2887–2901.

• Marquet P. (2011). Definition of a moist entropic potential temperature. Application to FIRE-I data flights. *Q. J. R. Meteorol. Soc.*, **137**: 768-791. `https://arxiv.org/abs/1401.1097`

• Marquet P. (2017). A Third-Law Isentropic Analysis of a simulated Hurricane. *J. Atmos. Sci.*, **74**, 3451–3471. `https://arxiv.org/abs/1704.06098`

• Marquet P. and Bechtold P. (2020). A new Estimated Inversion Strength (EIS) based on the moist-air entropy. *Research activities in Earth system modelling. Working Group on Numerical Experimentation. Report No. 50.* WCRP Report No.12/2020. WMO, Geneva `http://bluebook.meteoinfo.ru/`

• Marquet P. and Dauhut T. (2018). Reply to "Comments on 'A Third-Law Isentropic Analysis of a Simulated Hurricane'". *J. Atmos. Sci.*, **75**, 3735–3747. `https://arxiv.org/abs/1805.00834`

• Marquet P. and Geleyn J.-F. (2015). *Formulations of moist thermodynamics for atmospheric modelling*. Chapter 22 of the book "Parameterization of Atmospheric Convection" by R. S. Plant and J.-I. Yano, editors, Vol. 2: Current issues and new theories (p.221-274). World Scientific, Imperial College Press. `http://arxiv.org/abs/1510.03239`

• Pauluis O.M. and Mrowiec A.A. (2013). Isentropic Analysis of Convective Motions, *J. At mos. Sci.*, **70**, 3673–3688.

• Stevens B. and Siebesma A.P. (2020). *Clouds as Fluids.*. In A. Siebesma, S. Bony, C. Jakob, & B. Stevens (Eds.), Clouds and Climate: Climate Science's Greatest Challenge (pp. 35-73). Cambridge: Cambridge University Press.

Polar Lows: Statistical relationship between size and duration

Mokhov I.I.[1,2], Poroshenko A.G.[1]

[1]A.M. Obukhov Institute of Atmospheric Physics RAS

[2]Lomonosov Moscow State University

mokhov@ifaran.ru

Statistical estimates of the relationship between the characteristic sizes (R) and the lifetime (τ) of polar mesocyclones (Polar Lows, PL) were obtained according to STARS data (Sea Surface Temperature and Altimeter Synergy for Improved Forecasting of Polar Lows) for the period 2002-2010 [1] (see also [2]). STARS data, based on satellite infrared images obtained using the AVHRR (Advanced Very-High-Resolution Radiometer) instrument, characterize PL parameters over the Norwegian and Barents Seas with hourly resolution.

Figure 1 (a,b) shows characteristic PL maximum and mean size R [km] in dependence on PL duration τ [hours]: R = Rmax (a), R = Rmean (b). In Fig. 1, different branches can be distinguished for the relationship between the characteristic size and duration of PLs. In particular, it is possible to highlight the features of PLs with $R \leq 200$ km and with $R > 200$ km. Nonlinear features are displayed for the largest PLs in dependence on their duration.

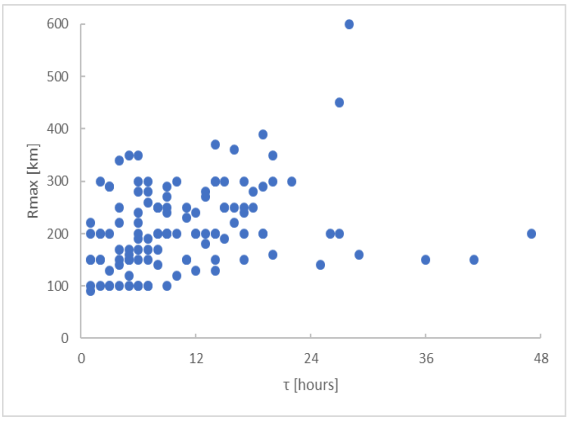

(a)

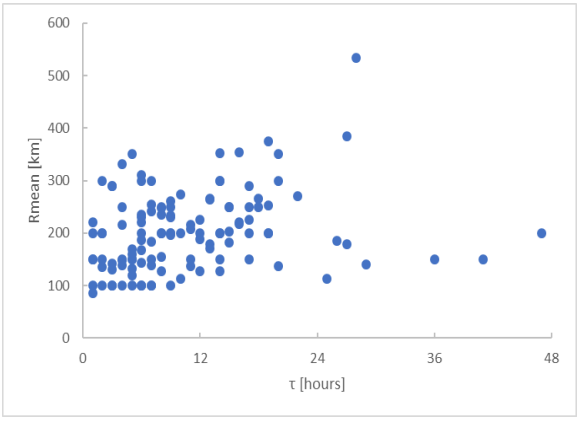

(b)

Fig. 1. Characteristic PL maximum and mean size R [km] as a function of PL duration τ [hours]: R=Rmax (a), R=Rmean (b).

Figure 2 (a,b) characterizes PL size R [km] (> 200 km) in dependence on PL duration τ [hours] on logarithmic scales: (a) *ln* Rmax vs ln τ, (b) *ln* Rmean vs *ln* τ. Linear regressions *ln* Rmax = a + k_M *ln* τ and *ln* Rmean = b + k_m *ln* τ (lines in Fig. 2) correspond to the dependences $R\text{max} \sim \tau^{k_M}$, $R\text{mean} \sim \tau^{k_M}$. Blue lines in Fig. 2 (a, b) characterize the linear regressions for all analyzed PLs with $R > 200$ km, red lines correspond to PL with $\tau > 12$ hours, green lines correspond to PL with $\tau > 18$ hours.

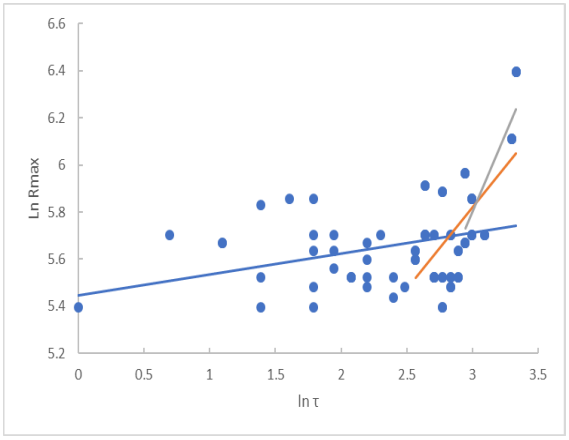

(a)
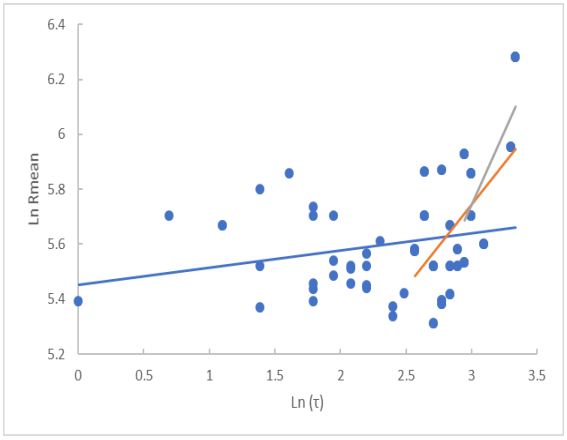

(b)

Fig. 2. Characteristic PL size *R* [km] (> 200 km) in dependence on PL duration τ [hours] : (a) *ln R*max vs *ln* τ, (b) *ln R*mean vs *ln* τ.

Table 1 presents the estimates of k_M and k_m with their standard deviations, as well as the correlation coefficients *r* for the corresponding linear regressions *ln R* on *ln* τ.

Table 1. Estimates of k_M and k_m with their standard deviations for the corresponding linear regressions *ln R* on *ln* τ (in brackets: correlation coefficients *r*)

R > 200 km	k_M (*r*)	k_m (*r*)
τ > 6 hours	0.09±0.04 (0.32)	0.06±0.04 (0.23)
τ > 12 hours	0.69±0.19 (0.64)	0.60±0.20 (0.55)
τ > 18 hours	1.30±0.43 (0.80)	1.07±0.50 (0.69)

The most statistically significant estimates of k_M and k_m were obtained for longer lived PLs (with k_m about 0.6 and k_M about 0.7 for PLs with τ > 12 hours and with k_m about 1.1 and k_M about 1.3 for PLs with τ > 18 hours).

The analysis of polar mesocyclones was carried out within the framework of the RSF project (19-17-00240).

References

[1] Noer G., Saetra Ø., Lien T., Gusdal Y. (2011) A climatological study of polar lows in the Nordic Seas. *Q. J. R. Meteorol. Soc.* **137**: 1762–1772.
[2] Akperov M.G., Mokhov I.I., Dembitskaya M.A. (2017) Arctic mesocyclones from satellite data and model simulations. *Current Problems in Remote Sensing of the Earth from Space*. **14** (3): 207-304. DOI:10.21046/2070-7401-2017-14-3-297-304

Impact of ice cloud treatment on the OLR in the radiation calculation of JMA global NWP model

Ryoji Nagasawa
Meteorological Research Institute / Japan Meteorological Agency
E-mail: r-nagasawa@mri-jma.go.jp

1. Introduction

There is a positive bias in outgoing longwave radiation (OLR) of the JMA global NWP model (Yonehara et al. 2020) (Fig. 1). There are several possible causes, one of which is the treatment of ice clouds in radiation calculations. To estimate the radiative forcing of an ice cloud, it is necessary to estimate its single scattering properties, for which an ice cloud optical property parameterization and an ice cloud effective size parameterization are required.

An accurate ice cloud optical property parameterization is contingent on high quality reference results. To fit the reference results with accuracy, it is necessary to use the definition of the effective size of ice clouds, which is more directly related to the formulation of the single scattering calculation of ice crystals. Since ice clouds are composed of nonspherical ice crystals, various definitions of the ice cloud effective size are used. For example, in the radiation scheme of atmospheric models, the definition of the ice cloud effective size in the ice cloud optical property parameterization may be different to that in the ice cloud effective size parameterization. The single scattering calculation depends strongly on the ice cloud effective size and it is therefore important that the definition is consistent.

Here we consolidate the definition of the ice cloud effective size in the radiation calculations of the JMA global NWP model, and test the improved ice cloud optical property parameterization and ice cloud effective size parameterization.

2. Ice cloud optical property parameterization

The current shortwave and longwave ice cloud optical property parameterization used in the JMA global NWP model is described by Ebert and Curry (1992) (hereafter EC92). In EC92, the reference calculation for the single scattering properties of ice crystals is based on the assumption that the shape of the ice crystals is a hexagonal column. The geometric optics approximation (for shortwave radiation) and the Mie scattering calculation (for longwave radiation) are employed. In EC92, the reference results are fitted using the ice cloud effective radius (ReEC), which is the radius of the sphere having the same surface area as the hexagonal column.

In this study, the ice cloud optical property parameterization of Fu (1996) used for shortwave radiation and Fu et al. (1998) used for longwave radiation are tested (hereafter collectively referred to as FU). The single scattering property reference results of FU are improved compared with EC92. This improvement arises from several factors, including the use of the improved imaginary part of the refractive ice index, more aircraft observations of the particle size distribution of ice clouds, a highly accurate geometric optics approximation, and the adoption of a composite method in the longwave radiation calculation through a combination of the geometric optics approximation and the Mie scattering calculation. In FU, the reference results are fitted using the generalized effective size (Dge). The fitting accuracy of the reference results is higher in Dge than in ReEC, because the definition of Dge is more directly related to the formulation of the reference calculation than is the definition of ReEC.

The accuracy of FU is higher than that of EC92. We find that the radiative forcing of ice clouds calculated using the FU scheme is smaller than that using the EC92 scheme (Fig. 2).

3. Ice cloud effective size parameterization

The current effective size parameterization for ice clouds used in the JMA global NWP model is described by Wyser (1998) (hereafter WY98). The WY98 scheme is based on the particle size distribution obtained from aircraft observations of midlatitude cirrus. The shape of ice crystals is assumed to be a hexagonal column and the effective radius of the ice cloud is based on the average radius of hexagonal columns randomly oriented in space (ReLiou). We note that ReLiou is inconsistent with ReEC.

In this study, the ice cloud effective size parameterization of Sun (2001) is tested (hereafter SUN01). The SUN01 scheme is based on the particle size distribution obtained from aircraft observations of anvil outflow in deep tropical convection (McFarquhar and Heymsfield 1997). The shape of ice crystals is also assumed to be a hexagonal column. The SUN01 scheme has been extended to be applicable to midlatitude cirrus through a comparison with observations. The definition of the ice cloud effective size in SUN01 is Dge, which is consistent with FU but not with EC92, so it is necessary to convert Dge to ReEC for use with EC92.

SUN01 is slightly more accurate than WY98. We find that the radiative forcing of ice clouds when using the SUN01 scheme is larger because the effective size of ice clouds tends to be smaller (Fig. 3).

4. Sensitivity experiments

When changing the ice cloud optical property parameterization from EC92 to FU, the positive bias of

OLR increases and the outgoing shortwave radiation (OSR) decreases in regions with many high-altitude clouds. This is because the radiative forcing of ice clouds calculated using the FU scheme is smaller than that using the EC92 scheme (Fig. 4, left panel).

When changing the ice cloud effective size parameterization from WY98 to SUN01, the positive bias of OLR is reduced and the OSR increases in regions with many high-altitude clouds. This is due to the larger radiative forcing of ice clouds in the SUN01 scheme compared to the WY98 scheme (Fig. 4, middle panel).

When combining the FU and SUN01 schemes (FUSUN01), their impacts have opposing effects and offset each other to some extent. As a result, the OLR increases only slightly in regions with many high-altitude clouds (Fig. 4, right panel).

5. Summary and outlook

We tested different ice cloud optical property parameterizations and ice cloud effective size parameterizations in the radiation scheme of the JMA global NWP model, ensuring that the definition of the ice cloud effective size was consistent in both parameterizations. The improved treatment of ice clouds in the FU and SUN01 schemes could not eliminate the positive OLR bias in the model. In future, we plan to investigate other causes of the OLR bias, such as the representation of high-altitude clouds.

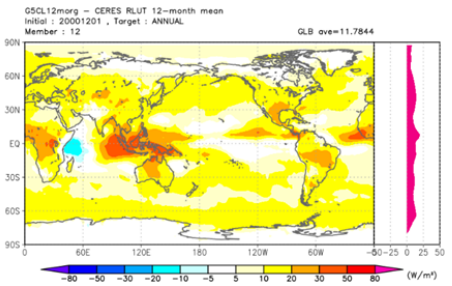

Fig. 1 The OLR bias (Wm^{-2}) in the JMA global NWP model after a 1-year integration (TL159L100, 12member) (CNTL-CERES).

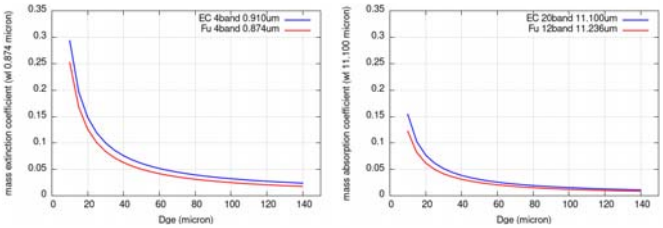

Fig. 2 Dge dependence of ice cloud optical properties using the FU scheme (red) and the EC92 scheme (blue); (left panel) mass extinction coefficient (m^2/g) near the wavelength of 0.9 μm, (right panel) mass absorption coefficient (m^2/g) near the wavelength of 11 μm.

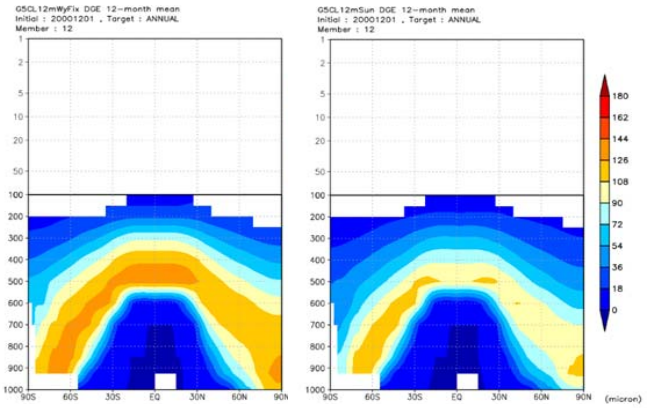

Fig. 3 Zonal mean generalized effective size, Dge (μm), in the JMA global NWP model after a 1-year integration (TL159L100, 12member). (left panel) WY98, (right panel) SUN01.

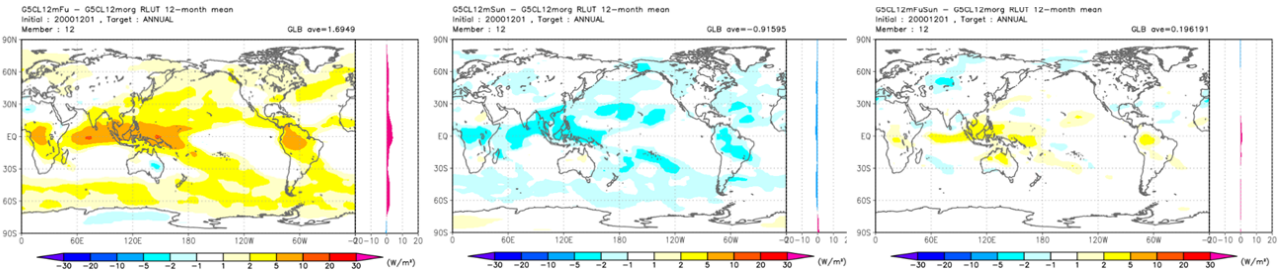

Fig. 4 The impact on the OLR (Wm^{-2}) in the JMA global NWP model after a 1-year integration (TL159L100, 12member); (left panel) FU-CNTL, (middle panel) SUN01-CNTL, (right panel) FUSUN01-CNTL.

References

Ebert, E. E., and J. A. Curry, 1992: A parameterization of ice cloud optical properties for climate models. *J. Gesphys. Res.*, **97**., 3831-3836.

Fu, Q., 1996: An accurate parameterization of the solar radiative properties of cirrus clouds for climate models. *J. Climate*, **9**, 2058-2082.

Fu, Q., P. Yang, and W. B. Sun, 1998: An accurate parameterization of the infrared radiative properties of cirrus clouds for climate models. *J. Climate*, **11**, 2223-2237.

McFarquhar, G. M., and A. J. Heymsfield, 1997: Parameterization of tropical cirrus ice crystal size distributions and implications for radiative transfer: Results from CEPEX. *J. Atmos. Sci.*, **54**., 2187-2200.

Sun, Z., 2001: Reply to comments by Greg M. McFarquhar on 'Parameterization of effective sizes of cirrus-cloud particles and its verification against observations' *Quart. J. Roy. Meteor. Soc*, **127**, 267-271.

Wyser, K., 1998: The effective radius in ice clouds. *J. Climate*, **11**, 1793-1802.

Yonehara, H., C. Matsukawa, T. Nabetani, T. Kanehama, T. Tokuhiro, K. Yamada, R. Nagasawa, Y. Adachi, and R. Sekiguchi, 2020: Upgrade of JMA's Operational Global Model. *CAS/JSC WGNE Res. Activ. Earth. System Modell.,* 6.19 –6.20.